

# Excitation Dephasing, Product Formation, and Vibrational Coherence in an Intervalence Charge-Transfer Reaction

David C. Arnett,<sup>\*,†</sup> Peter Vöhringer,<sup>‡</sup> and Norbert F. Scherer<sup>\*,§</sup>

Contribution from Department of Chemistry, University of Pennsylvania, Philadelphia, Pennsylvania 19104

Received January 6, 1995<sup>®</sup>

**Abstract:** The ultrafast dynamics associated with optically induced intervalence charge-transfer reactions in solution are investigated in the Fe<sup>II</sup>–Fe<sup>III</sup> complex Prussian blue. The experimental measurements, including frequency and polarization dependent pump probe studies, are performed using ultrashort (i.e. 20 fs) pulses generated by a home-built cavity-dumped Ti:sapphire laser. Complicated time-domain waveforms reflect the several different processes and time scales for the relaxation of coherences and populations in this extended solid. The degenerate Fe<sup>II</sup>–Fe<sup>III</sup> transitions as well as the octahedral symmetry of the excitation in the “colloidal” material yields a novel coherent response prior to back electron transfer as observed through the decay of optical anisotropy. Several low frequency Raman active vibrational modes that are coupled to the CT coordinate are detected. A sub-picosecond to picosecond time scale transient absorption feature is shown to reflect the formation of a new product state (i.e. relaxed CT state) that persists for tens of picoseconds. The results are interpreted as wavepacket motion on the ground and CT (i.e. excited) state potential energy surfaces exhibiting five dynamical processes: (1) rapid CT state electronic dephasing, (2) ground state vibrational dephasing, (3) population relaxation, (4) back electron transfer through vibrationally hot levels of the ground state electronic configuration, and (5) formation of the relaxed CT species.

## I. Introduction

Considerable progress has been made in recent years in understanding the interaction of a reacting system (i.e. chromophore) with the surrounding environment (i.e. bath).<sup>1,2</sup> This is a particularly challenging problem in the case where the bath is a liquid that responds on a series of time scales.<sup>3</sup> New experimental measurements and theoretical descriptions of solvent “friction” are enhancing the microscopic perspective and insight into chemical reactions. While dynamical solvent effects are of importance for dictating the time scale of reaction and energetics through, respectively, the prefactor and exponent of reaction rate expressions, internal motions coupled to the reaction coordinate also have to be considered. Elucidation of both contributions requires a variety of experimental methods and theoretical insights.<sup>4–8</sup>

The direct viewing of transient and even transition state species has become increasingly accessible to experimental measurement due to advances in the duration of ultrashort pulses, reliability of generation, and refinement of methodology.<sup>9</sup>

Such studies are even becoming a reality for chemical reactions in solution.<sup>10–12</sup> Time-domain approaches provide complementary, sometimes unique, information to frequency domain methods such as resonance Raman spectroscopy. The wavepacket picture of Raman spectroscopy<sup>13</sup> shows that this frequency domain technique is sensitive to rapid dynamics on time scales comparable to optical dephasing. In terms of vibrational dynamics, only the ground state modes (i.e. frequencies) whose excited state counterparts are displaced, possibly through coupling to the reaction, are detected. Excited state dynamics that involve recurring wavepacket motion are, however, not as amenable to study by this approach. The dynamics of product formation as well as excited state coherent oscillations are better examined in the time domain. However, both methods can be simultaneously applied particularly when the transient nature of a process allows only the briefest glimpse into the existence of the intermediate.<sup>14</sup> The complementary nature of time and frequency domain spectroscopies is currently being exploited in understanding optically induced chemical processes including charge-transfer.<sup>15–20</sup>

The optically induced metal-to-metal charge-transfer (MMCT) that occurs in mixed-valence compounds has been the focus of several ultrafast studies. These studies, typically employing

<sup>†</sup> Department of Education GAANN Predoctoral Fellow.

<sup>‡</sup> Deutsche Forschungsgemeinschaft Postdoctoral Fellow. Present address: Max Planck Institut für Biophysikalische Chemie, Tamannstrasse 6, D-37077, Göttingen, Germany.

<sup>§</sup> National Science Foundation National Young Investigator.

<sup>®</sup> Abstract published in *Advance ACS Abstracts*, December 1, 1995.

(1) Weaver, M. J.; McManis, G. E., III. *Acc. Chem. Res.* **1990**, *23*, 294.

(2) Maroncelli, M. *J. Mol. Liq.* **1993**, *57*, 1.

(3) Vöhringer, P.; Arnett, D. C.; Westervelt, R. A.; Feldstein, M. J.; Scherer, N. F. *J. Chem. Phys.* **1995**, *102*, 4027. Vöhringer, P.; Arnett, D. C.; Yang, T.-S.; Scherer, N. F. *Chem. Phys. Lett.* **1995**, *237*, 387.

(4) Joo, T.; Jia, Y.; Fleming, G. R. *J. Chem. Phys.* **1995**, *102*, 4063–4068.

(5) Marcus, R. A. *J. Chem. Phys.* **1956**, *24*, 966, 979. *Ibid.* **1956**, *43*, 679. Sumi, H.; Marcus, R. A. *J. Chem. Phys.* **1986**, *84*, 4894.

(6) Bixon, M.; Jortner, J. *J. Chem. Phys.* **1993**, *176*, 467–481.

(7) Vöhringer, P.; Westervelt, R. A.; Yang, T.-S.; Arnett, D. C.; Feldstein, M. J.; Scherer, N. F. *J. Raman Spectrosc.* **1995**, *26*, 535.

(8) Yang, T.-S.; Vöhringer, P.; Arnett, D. C.; Scherer, N. F. *J. Chem. Phys.* **1995**, *103*, 8346.

(9) Zewail, A. H. *J. Phys. Chem.* **1993**, *97*, 12427–12446. Khundkar, L.; Zewail, A. H. *Annu. Rev. Phys. Chem.* **1990**, *41*.

(10) Banin, U.; Kosloff, R.; Ruhman, S. *Isr. J. Chem.* **1993**, *33*, 141–156. Banin, U.; Ruhman, S. *J. Chem. Phys.* **1993**, *98*, 4391–4403.

(11) Johnson, A. E.; Levinger, N. E.; Barbara, P. J. *Phys. Chem.* **1992**, *96*, 7841–7844.

(12) Scherer, N. F.; Zeigler, L. D.; Fleming, G. R. *J. Chem. Phys.* **1992**, *96*, 5544. Scherer, N. F.; Jonas, D.; Fleming, G. R. *Ibid.* **1993**, *99*, 153.

(13) Tannor, D.; Sunberg, H. *J. Phys. Chem.* **1986**, *86*, 1822. Heller, E. *Acc. Chem. Res.* **1981**, *14*, 368. Myers, A. B.; Mathies, R. A. *J. Chem. Phys.* **1984**, *82*, 1552.

(14) Myers, A. B. *J. Opt. Soc. B.* **1990**, *7*, 1665–1672.

(15) Walker, G. C.; Barbara, P. F.; Doorn, S. K.; Dong, Y.; Hupp, J. T. *J. Phys. Chem.* **1991**, *95*, 5712.

(16) Tominaga, K.; Klinier, D. A. V.; Johnson, A. E.; Levinger, N. E.; Barbara, P. F. *J. Chem. Phys.* **1993**, *98*, 1228–1243.

(17) Klinier, D. A. V.; Tominaga, K.; Walker, G. C.; Barbara, P. F. *J. Am. Chem. Soc.* **1992**, *114*, 8323–8325.

(18) Doorn, S. K.; Stoutland, P. O.; Dyer, R. D.; Woodruff, W. H. *J. Am. Chem. Soc.* **1992**, *114*, 3133.

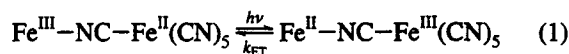
pump-probe techniques, have greatly assisted in the elucidation of the dynamics involved in electron transfer processes in solution. Important observations include the direct detection of reverse reaction rates,  $k_{ET}$ ,<sup>15</sup> evidence for intramolecular and solvent contributions to the dynamics,<sup>19</sup> and detection of vibrational relaxation.<sup>20</sup> Despite these advances, intramolecular vibrational coherences have only recently been observed in time-domain measurements of MMCT reactions.<sup>19</sup> By contrast, vibrational modes (frequencies) and their contribution to inner-sphere reorganization (Huang–Rhys factor,  $S_j$ , for each mode  $j$  in CT and MMCT) have been characterized by resonance Raman (RR) methods.<sup>21,22</sup> The cw-RR technique is most applicable to high frequency modes, whereas time-domain approaches should be most sensitive to low frequency vibrational modes below 1000  $\text{cm}^{-1}$  and to solvent (i.e. outer sphere) reorganization.

This paper presents time resolved pump-probe measurements of the optically induced charge-transfer and the subsequent back reaction of the  $\text{Fe}^{\text{II}}\text{--Fe}^{\text{III}}$  mixed valence compound Prussian blue in aqueous solutions. Here, the excitation (or pump) pulse induces a direct electron transfer from an  $\text{Fe}^{\text{II}}$  ion to adjacent  $\text{Fe}^{\text{III}}$  sites. The relaxation of the excited CT state, formation of the relaxed CT-state products, and recovery of the Prussian blue ground state is then detected with a probe pulse as a function of time, electric field polarization vector (relative to the pump pulse), and frequency. These high signal to noise pump probe studies with vibrationally-impulsive pulses provide temporal, spectral, and spatial information about the excitation and relaxation dynamics of the intervalence charge-transfer process. The results yield information about the relaxation of electronic coherence as well as vibrational coherences vis-a-vis wavepacket motion in the CT state and ground states, respectively.

The paper is organized into background, experimental, results, and discussion sections. Section II provides background information about the nature of the charge-transfer transition, structure, and symmetry of Prussian blue in solution. The Experimental Section (III) gives a description of the cavity-dumped Ti:sapphire laser that was developed for these studies as well as the pump-probe setup. Section IV presents the results of pump-probe, polarization anisotropy, and wavelength resolved measurements. The different dynamical processes contributing to the temporal response and anisotropy decay are discussed in section V. The paper concludes with remarks about additional experimental studies that are necessary to verify the nature of the electronic dephasing process in this octahedral extended solid.

## II. Background

Prussian blue, the classic mixed valence hexacyanide, received its name as a result of the intense blue color that it exhibits in both the crystalline and aqueous form due to a broad MMCT absorption band at 700 nm.<sup>23</sup> The MMCT and the back electron transfer process can be represented as:



(19) Reid, P. J.; Silva, C.; Dong, Y.; Hupp, J. T.; Barbara, P. F. *Ultrafast Phenomena*, Vol. 7; OSA Technical Digest Series 255; 1994. Private Communication. Reid, P. J.; Silva, C.; Barbara, P. F.; Karki, L.; Hupp, J. T. *J. Phys. Chem.* **1995**, *99*, 2609–2616.

(20) Stoutland, P. O.; Doorn, S. K.; Dyer, R. B.; Woodruff, W. H. *Ultrafast Phenomena*, Vol. 7; OSA Technical Digest Series, 1994.

(21) Markel, F.; Ferris, N. S.; Gould, I. R.; Myers, A. B. *J. Am. Chem. Soc.* **1992**, *114*, 6208.

(22) See Todd, M. D.; Nitzan, A.; Ratner, M. A.; Hupp, J. T.; *J. Photochem. Photobiol. A: Chem.* **1994**, *82*, 87 and references therein.

(23) Robin, M. B.; Day, P. *Adv. Inorg. Chem. Radiochem.* **1967**, *10*, 247. Robin, M. B. *Inorg. Chem.* **1962**, *1*, 337.

In the crystalline form, Prussian blue assumes a face centered cubic structure with each  $\text{Fe}^{\text{II}}$  ion octahedrally surrounded by the carbon ends of the cyanide ligands and each  $\text{Fe}^{\text{III}}$  ion located in an octahedral hole formed by the nitrogen ends. Hence, with reference to Figure 1, each central  $\text{Fe}^{\text{II}}$  ion is surrounded by six  $\text{Fe}^{\text{III}}$  ions, all of which participate in the electron transfer process represented by eq 1. The iron structure of the octahedral subunit  $\text{Fe}^{\text{II}}(\text{CN})_6\text{Fe}_6^{\text{III}}$  is shown in Figure 1 where the bridging CN ligands have been omitted for clarity. In solution, Prussian blue easily peptizes to form a (colloidal) suspension which provides an octahedral network similar to that observed in the solid. The resulting extended network is expected to play an important role in the ultrafast dynamics. It is worth noting that the compound considered in this study is in fact an extended network solid as opposed to the  $(\text{CN})_5\text{Fe}^{\text{III}}\text{NCFe}^{\text{II}}(\text{CN})_5$  dimer which exhibits a MMCT absorption at 1300 nm.<sup>24</sup>

## Structure of Prussian Blue

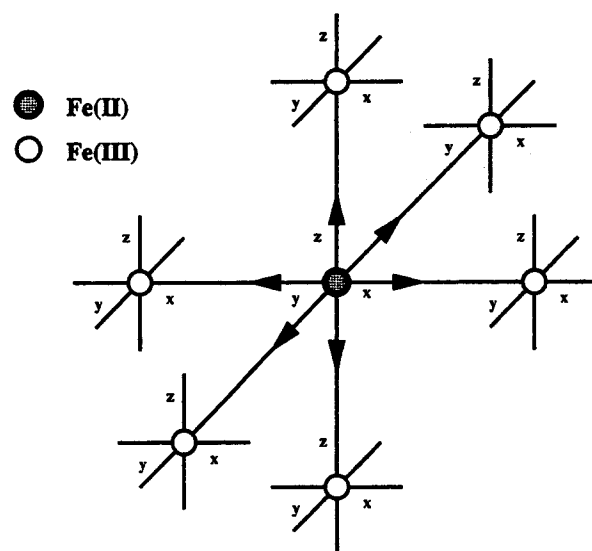
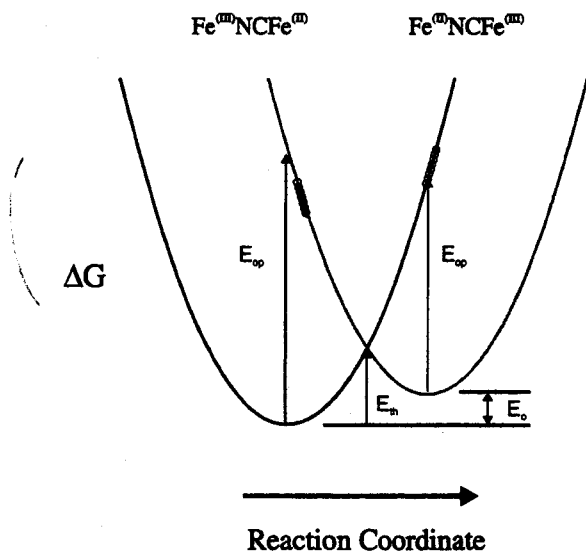


Figure 1. Schematic of the octahedral structure of Prussian blue consisting of  $\text{Fe}^{\text{II}}$  sites (shaded circles) bridged by CN to  $\text{Fe}^{\text{III}}$  sites.

Static electronic absorption spectroscopy and molecular orbital calculations suggest that Prussian blue is a class (II) mixed valence compound with the optical electrons largely (99%) localized on the  $\text{Fe}^{\text{II}}$  ions in the ground state.<sup>23</sup> The  $\text{Fe}^{\text{II}}$  ions in the carbon holes have a low-spin, strong-field configuration with all six of the d-electrons occupying  $t_{2g}$  orbitals, which lie in the three orthogonal planes defined by the six cyanide ligands. The  $\text{Fe}^{\text{III}}$  ions in the nitrogen holes have a high-spin low-field configuration with three d-electrons occupying the  $t_{2g}$  orbitals and two d-electrons occupying the higher energy  $e_g$  orbitals. MMCT excitation corresponds to promotion of an electron from a  $t_{2g}$  orbital of the  $\text{Fe}^{\text{II}}$  ion, situated in the carbon hole, to a half filled  $t_{2g}$  orbital of the  $\text{Fe}^{\text{III}}$  ion in the nitrogen hole. Consideration of the number of possible donating and accepting orbitals yields 54 approximately degenerate transitions for optical electron transfer.<sup>23</sup>

The free energy curves of the ground state ( $\text{Fe}^{\text{III}}\text{NCFe}^{\text{II}}$ ) and excited state ( $\text{Fe}^{\text{II}}\text{NCFe}^{\text{III}}$ ) are illustrated in Figure 2. Here, the charge-transfer is considered to be a nonadiabatic process although, in principle, the curves should be adjusted to reflect

(24) Day, P. *Comments Inorg. Chem.* **1981**, *1*, 155–167. Mayoh, B.; Day, P. *J. Chem. Soc., Dalton Trans.* **1974**, *1974*, 846.



**Figure 2.** Free energy diagram for the ground  $\text{Fe}^{\text{III}}\text{NCFe}^{\text{II}}$  and excited  $\text{Fe}^{\text{II}}\text{NCFe}^{\text{III}}$  electronic configurations.  $E_{\text{op}} = 14100 \text{ cm}^{-1}$ ,  $E_{\text{th}} = 4033 \text{ cm}^{-1}$ ,  $E_0 = 1776 \text{ cm}^{-1}$ , and  $E_{\text{op}}^* = 12324 \text{ cm}^{-1}$ . The circles represent the window of observation available with the laser center wavelength and bandwidth. The arrows represent the absorption maxima for the two  $\text{Fe}^{\text{II}}\text{Fe}^{\text{III}}$  structures.

the electronic mixing between the states.<sup>23</sup> Experimental observations have established the optical transition energy in solution,  $E_{\text{op}}$ , to be  $14100 \text{ cm}^{-1}$ <sup>23</sup> and the thermal activation energy,  $E_{\text{th}}$ , as  $4033 \text{ cm}^{-1}$ .<sup>25</sup> Using these parameters, and following the treatment of Hush and others for nonsymmetric mixed valence charge-transfer systems,<sup>22,26</sup> the energy difference between the two states  $E_0$  becomes  $1776 \text{ cm}^{-1}$ . Assuming harmonic oscillator (i.e. parabolic) potential energy surfaces with different minima and the same curvature, the energy for an optical transition from the excited state ( $\text{Fe}^{\text{II}}\text{NCFe}^{\text{III}}$ ) to the ground state ( $\text{Fe}^{\text{III}}\text{NCFe}^{\text{II}}$ ),  $E_{\text{op}}^*$ , would be red-shifted from  $E_{\text{op}}$  by the energy difference between the two free energy curves,  $E_0$ , and has the value  $E_{\text{op}}^* = E_{\text{op}} - E_0 = 12324 \text{ cm}^{-1}$ . The circled areas shown on the excited state free energy surfaces in Figure 2 represent the window of observation accessible with the laser center wavelength and bandwidth used for the present experiments. This region is to the red of the metal-to-metal charge-transfer transition energy,  $E_{\text{op}}$ , but may reflect a transient absorption between the relaxed CT state and the vertically displaced ground state at  $E_{\text{op}}^*$ .

The nature of the electronic transition within a subunit of Prussian blue ( $\text{Fe}^{\text{III}}\text{NC})_6\text{Fe}^{\text{II}}$  which has  $O_h$  symmetry, has been studied within the framework of group theory and molecular orbital calculations by Day.<sup>24</sup> The octahedral symmetry of the complex about the carbon hole provides three mutually orthogonal transition moments for electron transfer along the axes of the bridging cyanide ligands. Here, the ground electronic state is a linear combination of metal-metal, ligand-metal, and ligand-ligand configurations of  $A_{1g}$  symmetry. Optically active excited states are formed as linear combinations of  $T_{1u}$  symmetry states. Hence the optical transition converts the system from a totally symmetric configuration to a combination of states that have symmetry similar to that of the transition dipole moments.<sup>24</sup>

When a sample containing Prussian blue is irradiated with polarized light, the probability of exciting the MMCT is proportional to the square of the projection of the transition moments. This projection is determined by the overlap of the

$t_{2g}$  donating and accepting orbitals onto the polarization axis of the incident electric field. Although the excited state will contain contributions from all three degenerate dipoles, the initial excited state will be a coherent superposition of electronic states with a net molecular transition dipole that is aligned with the polarization of the incident beam. The prepared state takes on the symmetry of the product of dipolar ( $T_{1u}$ ) and molecular (i.e. octahedral  $O_h$ ) groups; in this case this product reduces to the dipolar group.

Differential thermal analysis of (insoluble) Prussian blue<sup>27</sup> has identified three different types of water molecules that exist within the octahedral network: zeolitic, lattice, and coordinated. The coordinated waters bond directly to  $\text{Fe}^{\text{III}}$  sites displacing a cyanide ligand, lattice waters form hydrogen bonds with the directly bonded coordinated water molecules, and zeolitic molecules bond indirectly to  $\text{Fe}^{\text{III}}$  sites through the other two intervening types of water. Ludi et al.<sup>26</sup> have shown that the coordination of the  $\text{Fe}^{\text{III}}$  ions can vary from  $\text{FeN}_4\text{O}_2$ , where 2 CN ligands have been displaced by  $\text{H}_2\text{O}$ , to  $\text{FeN}_6$ , yielding an average composition of  $\text{FeN}_{4.5}\text{O}_{1.5}$ . In other words, the natural water content of insoluble solid Prussian blue is sufficient to displace one-fourth of the cyanide ligands in the octahedral complex. Such substitutions can be thought of as a type of defect that reduces the local symmetry within the solid lattice. For soluble Prussian blue in water, the  $\text{H}_2\text{O}$  coordination is expected to be at least as prevalent. This may have the effect of reducing the symmetry of the system and destroying the true degeneracy of the  $t_{2g}$  orbitals. Certainly, the surface of the colloids in solution will be water-terminated.

### III. Experimental Section

The experimental set-up consists of a home-built cavity-dumped Ti:sapphire laser, dispersion compensation optics, beam-splitters and optical delay lines for pump-probe beams, polarization and focusing optics, and a flowing sample cell. The detection system consists of a monochromator, photomultiplier tube, lock-in amplifier, and computer. Details of the experimental system are given in the following subsections. A more detailed description of the design and performance of the cavity-dumped Ti:sapphire laser and comparison with other designs recently reported<sup>29,30</sup> is given elsewhere.<sup>31</sup>

**A. Cavity-Dumped Ti:Sapphire Laser.** The laser, shown in Figure 3, is a standard X-fold cavity that has been adapted to allow for cavity dumping. The Ti:sapphire laser (4.5 mm rod, 60 cm fused silica prism spacing) was based on the designs of Kaptien<sup>32</sup> and Krausz et al.<sup>33</sup> and routinely produces pulses of 15–20 fs duration.<sup>34</sup> This "standard" oscillator design was converted to a cavity-dumped oscillator by positioning an acousto-optic Bragg cell and curved reflectors in a X-fold configuration in the nondispersive arm of the cavity. The addition of the cavity dumper allows deflection of up to 80% of the intracavity energy out of the oscillator, yielding high energy pulses (30–50 nJ/pulse) at variable repetition rates with 15–20 fs pulse durations. For the measurements reported below, the repetition rate

(27) Bal, B.; Ganguli, S.; Bhattacharya, M. *J. Phys. Chem.* **1984**, *88*, 4575. Ganguli, S.; Bhattacharya, M. *J. Chem. Soc., Faraday Trans. 1* **1983**, *79*, 1515.

(28) Ludi, A.; Güdel, H. U. *Struct. Bonding* **1973**, *14*, 1. Buser, H. J.; Schwarzenbach, D.; Peter, W.; Ludi, A. *Inorg. Chem.* **1992**, *16*, 2704. Herren, F.; Fischer, P.; Ludi, A.; Hälg, W. *J. Chem. Soc., Dalton Trans.* **1980**, *19*, 956.

(29) Ramaswamy, M.; Ulman, M.; Paye, J.; Fujimoto, J. G. *Opt. Lett.* **1993**, *18*, 1822.

(30) Pschenichnikov, M. S.; de Boeij, W. P.; Weirsm, D. A. *Opt. Lett.* **1994**, *19*, 572.

(31) Arnett, D. C.; Scherer, N. F. *Opt. Lett.* **1995**, submitted.

(32) Asaki, M. T.; Huan, C. P.; Garvey, D.; Zhou, J.; Kapteyn, H. C.; Murnane, M. M. *Opt. Lett.* **1993**, *18*, 977.

(33) Krausz, F.; Spielmann, C.; Brabec, T.; Wintner, E.; Schmidt, A. J. *Opt. Lett.* **1992**, *17*, 204.

(34) Vöhringer, P.; Scherer, N. F. *J. Phys. Chem.* **1995**, *99*, 2684. Vöhringer, P.; Westervelt, R. A.; Yang, T.-S.; Arnett, D. C.; Feldstein, M. J.; Scherer, N. F. *J. Raman Spectrosc.* **1995**, *26*, 535.

(25) Hush, N. S. *Prog. Inorg. Chem.* **1967**, *8*, 391.

(26) Hush, N. S. *Electrochim. Acta* **1968**, *13*, 1005. Ludi, A. *Mixed-Valence Compounds*; Brown, D. B., Ed.; Reidel: London, 1979; p 151.

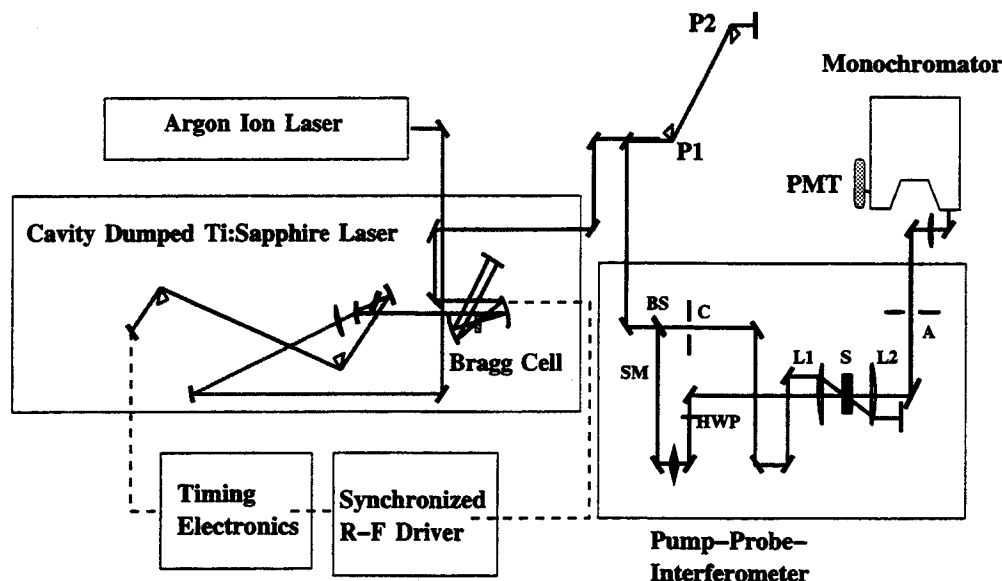


**Figure 3.** Experimental setup. BS = beam splitter, PMT = photomultiplier tube, P1 and P2 = compensating prisms, SM = scanning delay line, C = chopper, S = sample flow cell, L1 and L2 = 6 cm focal length achromat lenses, A = aperture.

was set at 250 kHz with 50% dumping efficiency. The resulting reduced repetition rate and lower average power (i.e. 10 mW) as compared with typical values for a standard oscillator with an output coupler (i.e. 90 MHz, 500 mW) serves to avoid thermal contributions to the measured signals, even in simple flow cells. The 30–50 nJ/pulse energies make the nonlinear optical measurements presented in this paper possible.

**B. Pump-Probe Scheme.** Following extra-cavity prism-pair chirp compensation, the diffracted beam contains transform limited pulses of 20 fs duration with energies in excess of 30 nJ/pulse. The spectral output of the laser, shown as the dashed trace in Figure 4, is centered at 780 nm with a bandwidth greater than 50 nm. For comparison, the absorption spectrum of aqueous Prussian blue is shown as the solid trace. As is apparent in this figure, the laser spectrum is shifted 80 nm to the red of the absorption maximum at 700 nm ( $\epsilon_{700} \approx 10000 \text{ M}^{-1} \text{ cm}^{-1}$ ). However, the molar extinction coefficient over the wavelength region spanned by the laser ( $\epsilon_{780} \approx 7000 \text{ M}^{-1} \text{ cm}^{-1}$ ) is adequate for pump-probe measurements with high-energy cavity-dumped pulses.

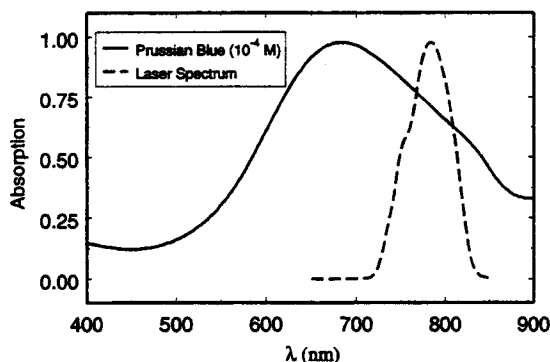


**Figure 4.** Absorption spectrum of Prussian blue in  $\text{H}_2\text{O}$  (solid traces) and in comparison to the laser spectrum (line-dots). The laser spectrum is centered 80 nm to the red of the absorption maximum.

The cavity-dumped pulse train is split into pump and probe beams with an intensity ratio of 4:1 and focused into a 0.5 mm flow cell which contains the samples of Prussian blue in  $\text{H}_2\text{O}$ . The sample optical density was adjusted to 0.3 or less. In all measurements the pump-induced modulation of the probe beam is detected using a photomultiplier tube, processed in a digital lock-in amplifier referenced to the chopped pump beam, and stored in an IBM-compatible 486 computer.

The polarization-dependent studies were conducted by inserting a half wave plate in the pump arm of the interferometer and adjusting

the polarization of the pump beam to an angle of  $0^\circ$  or  $90^\circ$  relative to the polarization of the probe beam. The frequency-resolved measurements were performed by dispersing the probe beam in a 0.25 m monochromator (Spex) with a 2 nm spectral window. The pump probe signal was measured at 10 nm intervals with another photomultiplier (Hamamatsu R928).

## IV. Results

**A. Polarization and Chirp-Dependent Studies.** Pump-probe signals of Prussian blue in  $\text{H}_2\text{O}$  are shown in Figure 5a for both parallel  $S_{||}(t)$  and perpendicular  $S_{\perp}(t)$  relative polarizations. The signal resulting from parallel polarizations shows a

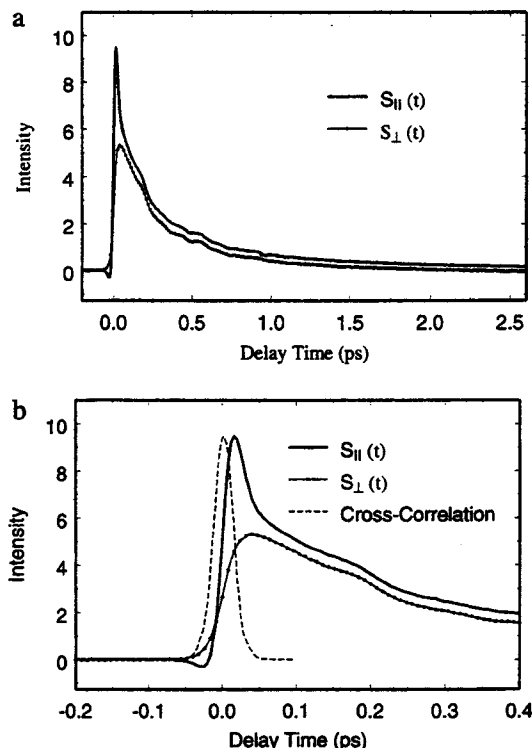


**Figure 5.** (a) Pump probe signals of Prussian blue in water using parallel (solid line) and perpendicular (line-dots) polarized pump and probe beams. (b) Expanded view of the early time behavior and instrument response function (dashed; cross-correlation).

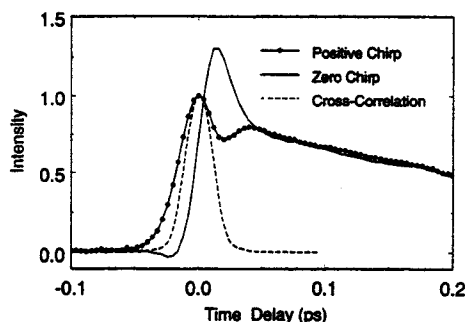


**Figure 6.** Pump probe signals ( $S_{||}$ ) obtained with chirped pulses (line with circles) and transform limited pulses (solid line). The chirped signal shows a coherence feature at  $T = 0$  as determined by the instrument response function (dashed trace), while the transform limited signal exhibits an artifact-free response.

rapid initial decay and a slower nonexponential relaxation with superimposed oscillations. When the excited complex is probed with a polarization perpendicular to that of the excitation pulse, the observed signal,  $S_{\perp}(t)$ , shows the same long time response as  $S_{||}(t)$  but the early time behavior is markedly different. A comparison of early time behavior is shown in Figure 5b and reveals that  $S_{\perp}(t)$  grows in as  $S_{||}(t)$  undergoes a rapid decay. This trend is more apparent in the deconvoluted data shown below.

The peak of the parallel signal shown in Figure 5b occurs after  $T = 0$ . The shift of the maximum of the parallel signal from  $T = 0$  indicates that the prompt component is not the result of an electric field coherence artifact. This is further confirmed by comparing signals obtained with chirped and unchirped pulses; these results are shown in Figure 6. The amount of material in the pump and probe arms is made equal so that the single prism compensation scheme will optimize or chirp both pulses. Therefore, the measurements yielding the two curves in Figure 6 have identical zero-of time-positions (as verified through the cross-correlation process) but are positively chirped or unchirped. The signal obtained with positively chirped pulses shows a spike feature centered at the maximum of the associated pump-probe cross-correlation response. By contrast, when the amount of material in the prism compensation setup is adjusted to properly compensate for the pulse chirp by translating the prism out of the beam, the peak shifts noticeably toward positive time and acquires a form similar to that shown in Figure 5 for  $S_{||}(t)$ . Therefore, the positively chirped pump-probe signal has a maximum coincident in time with the  $T = 0$  of the cross-correlation, whereas the rise of the optimized pump-probe signal follows the integral of the cross-correlation with an inflection point at  $T = 0$ . Further comparison of the waveforms shows that the positively chirped signal decays from the  $T = 0$  maximum has a small dip and rises to a signal level coincident with the unchirped pulse signal. This latter signal, again for parallel polarizations, actually exhibits a maximum at approximately the time of the dip observed in the chirped pulse case. The fast decay in the zero-chirp signal reflects genuine molecular dynamics and not electric field coherence effects. The pulse chirp only affects the short-time dynamics, and the signals become identical after 50 fs delay.

The rapid dynamics observed, we will argue below, result from rapid excited (i.e. CT) state relaxations that are probed by a stimulated emission process. The significance of the observation is the demonstration of experimental sensitivity to rapid excited state dynamics that involve electronic dephasing and system free energy relaxation.

**B. Deconvoluted Responses and Anisotropy.** The relaxation dynamics of  $S_{||}(t)$  and  $S_{\perp}(t)$  are analyzed by deconvoluting

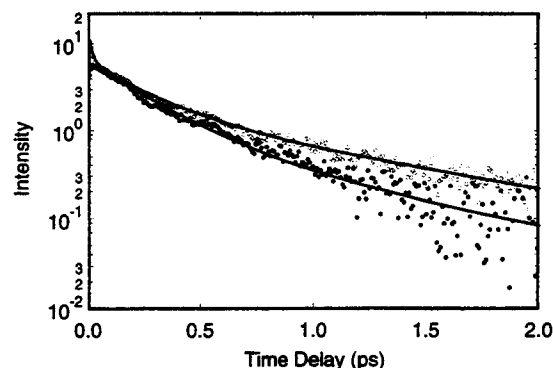


**Figure 7.** Deconvoluted pump probe data and multiexponential fit obtained for  $D_{||}$  (a) and  $D_{\perp}$  (b). The data are represented by circles (parallel, empty; perpendicular, solid) and the fits are shown as solid lines. The fitting parameters are given in the text. Only every other data point is shown.

the observed signals with the instrument response function obtained from the pump-probe cross-correlation. This deconvolution is performed in the frequency domain by dividing the Fourier transform of each time-domain data set, (i.e.  $S_{||\perp}(t)$ ) by the pump probe cross-correlation,  $A(t)$ , and inverse Fourier transforming the quotient,

$$D_{||\perp}(t) = \mathcal{F}^{-1} \left\{ \frac{\mathcal{F}[S_{||\perp}(t)]}{\mathcal{F}[A(t)]} \right\} \quad (2)$$

Here,  $\mathcal{F}$  represents the Fourier transformation operator, and  $\mathcal{F}^{-1}$  the inverse transformation operator. The decaying deconvoluted signal is then fit to a series of (i.e. three) exponentials, each representing different relaxation processes. The deconvoluted data and fits are shown for  $D_{||}(t)$  and  $D_{\perp}(t)$  in Figure 7. The semilog plot clearly shows that the decays occur on multiple time scales. Three exponential components, corresponding to short ( $15 \pm 5$  fs), medium ( $240 \pm 40$  fs), and longer ( $950 \pm 40$  fs) time scale dynamics, are necessary to reproduce the decay of  $D_{||}(t)$ .  $D_{\perp}(t)$  is fitted with a fast rising component ( $15 \pm 5$  fs) along with a biexponential decay with time constants of  $250 \pm 40$  and  $900 \pm 40$  fs; note that the fitted time constants are very similar for  $D_{||}(t)$  and  $D_{\perp}(t)$ .

The rapid component that is observed in the parallel signal in Figure 5 can be more clearly identified through the decay of the polarization anisotropy,<sup>35</sup> which is calculated as

$$r(t) = \frac{S_{||}(t) - S_{\perp}(t)}{S_{||}(t) + 2S_{\perp}(t)} \quad (3a)$$

or

$$r_D(t) = \frac{D_{||}(t) - D_{\perp}(t)}{D_{||}(t) + 2D_{\perp}(t)} \quad (3b)$$

for the deconvoluted signals. This anisotropy is shown in Figure 8 for both the raw and deconvoluted data. The anisotropy calculated from the unprocessed experimental data reaches a maximum of 0.33 at  $T = 8$  fs and decays to a small ( $r(t) \leq 0.05$ ) constant level within 50 fs. However, when the finite time resolution of the experiment is taken into account through FFT deconvolution with the instrument response function, the anisotropy reaches the classically allowed maximum<sup>35</sup> of 0.4 at  $T = 4$  fs and decays to a constant level within 30 fs. This fast decay of the anisotropy indicates that the excited state

(35) Fleming, G. R. *Ultrafast Studies of Chemical Dynamics*; Oxford Univ. Press: New York, 1986.

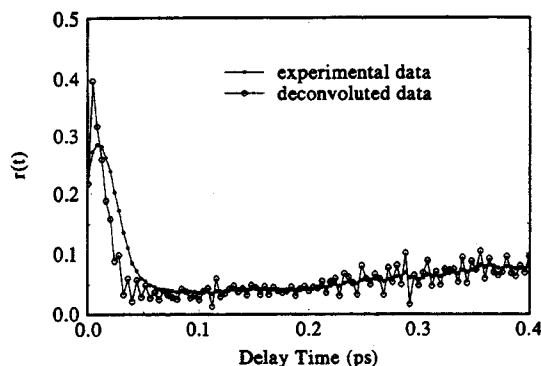


Figure 8. Time dependent anisotropy of Prussian blue in  $\text{H}_2\text{O}$  as calculated by eq 2 using both raw,  $r_S(t)$ , and deconvoluted data,  $r_D(t)$ .  $r_S(t)$ : line-solid circles,  $r_D(t)$ : line-open circles.

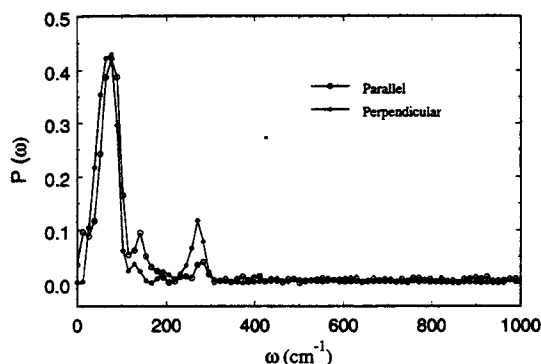


Figure 9. Fourier power spectrum obtained from  $S_{||}(t)$  (line and open circles) and  $S_{\perp}(t)$  (line and solid circles).

undergoes a rapid spatial or orientational relaxation, evolving from a configuration that is most readily probed with parallel polarized light to a configuration whose amplitude is nearly equally likely to be detected using a perpendicularly polarized probe. The decay of the deconvoluted anisotropy is well fit (except for the  $T = 0$  fs point) using a single exponential with a time constant of  $15 \pm 5$  fs. For the degenerate frequency case, an anisotropy value of zero indicates the creation of a spatially isotropic ground state hole and excited state configuration. Population relaxation does not affect the value of the anisotropy since both experimental configurations would experience the same amount of signal reduction.

Figure 9 shows the power spectra associated with  $D_{||}(t)$  and  $D_{\perp}(t)$  obtained through Fourier transformation of the deconvoluted data with the multiexponential fit subtracted. This identifies the two major oscillatory components at  $75 \text{ cm}^{-1}$  and  $270 \text{ cm}^{-1}$ . Linear prediction singular value decomposition (LPSVD) analysis<sup>36</sup> obtains the same frequencies and gives relaxation times of 60 and 600 fs for these modes, respectively. Short-pulse excitation may result in impulsive preparation of low frequency modes where the energy level spacing is less than the pulse spectrum bandwidth. Preparation of vibrational nonstationary states in the ground and excited electronic states are possible within each molecule of the ensemble that interacts with the optical pulses.<sup>37</sup> The  $270 \text{ cm}^{-1}$  feature is associated with a Fe-CN-Fe heavy-light-heavy motion of the CN that has been observed in far-IR spectra of solution-phase Prussian blue (this motion has contributions from both  $T_{1u}$  and  $T_{2u}$  symmetry elements).<sup>38</sup> The  $70 \text{ cm}^{-1}$  feature may result from

relative motions of the iron ions within the lattice although there is no independent proof of such an assignment since such low-frequency modes are not easily measured by IR or cw-Raman spectroscopy, for example, and have not, to our knowledge, been reported for this chemical system.

**C. Wavelength Resolved Studies.** Pump-probe signals obtained by spectrally dispersing the probe beam and detecting each individual wavelength component are shown in Figure 10. The 3-dimensional grayscale representation of the parallel polarized data shows the prominent ultrafast component (light grey), intermediate time scale relaxations (medium grey-black), and the superimposed oscillations. The frequency and time-resolved data reveals two characteristics of the transient that are not observable through frequency integrated techniques: the spectral behavior of the oscillatory components observed over all wavelengths, and the bifurcation of the transient into a bleach and an absorption component.

The oscillatory component, corresponding mainly to the  $270 \text{ cm}^{-1}$  mode observed in the Fourier spectra shown earlier, exhibits a wavelength dependent phase shift as determined through LPSVD analysis. A monotonic increase in phase angle with wavelength is found, consistent with the idea that the spectrum of the ground state vibrational wavepacket shifts to the red then to the blue. In other words, the oscillations are observed with the reddest portions of the pulse earlier than with the bluer portions. This is consistent with the results of wavepacket simulations of nonlinear spectroscopy for displaced harmonic potentials.<sup>37</sup> Similar wavelength-dependent phase-angle behavior is expected for measurements with the resonance conditions relevant to this experiment.<sup>36b</sup> A more detailed analysis of the amplitude and phase of the exponentially damped cosine curves observed in wavelength-resolved pump-probe measurements and the relation to oscillator displacement will be reported elsewhere.<sup>39</sup>

The bifurcation of the wavelength-resolved pump-probe measurements into separate bleach and absorption components is clearly illustrated in the three-dimensional greyscale representation of the time and wavelength-resolved data shown in Figure 10. Here, the grey portion of the plot shows the decay of a bleach (positive signal) while the black portion of the transient signal corresponds to a transient absorption (negative signal). These processes are also evident in Figure 11 where the pump-probe spectrum is shown for various delay times along with fits for each individual spectrum based on a simple model which will be described later in the text. These scans are not normalized to the finite probe pulse spectrum since this results in a divergence in the extreme red and blue frequency components. The earlier delay time spectra are dominated by the ground state transient bleach, which is reflected in the positive signal intensity. The wavelength-resolved signal observed at 100 fs time delay, long enough for the ultrafast response discussed above to completely decay, is very similar to the probe pulse spectrum. For delay times shorter than about 0.5 ps, a transient absorption (negative signal) begins to develop in the longer wavelength portion of the time-dependent spectra. At longer delay times, the transient feature evolves with a maximum negative signal centered between 805 and 810 nm. The magnitude of the transient absorption reaches a maximum at slightly less than 1 ps and does not decay on the time scales of these measurements. Longer time scans (not shown) indicate that the transient absorption feature begins to dissipate on a 10 ps time scale. The transient absorption feature could be

(36) (a) Wise, F. W.; Rosker, M. J.; Milhauser, G. L.; Tang, C. L. *IEEE J. Quantum Electron* 1987, QE23, 1116. (b) Walmsley, I. A.; Wise, F. W.; Tang, C. L. *Chem. Phys. Lett.* 1989, 154, 315.

(37) Pollard, W. T.; Lee, S. Y.; Mathies, R. A. *J. Chem. Phys.* 1990, 92, 4012. Pollard, W. T.; Dexheimer, S. L.; Wang, Q.; Peteau, L. A.; Shank, C. V.; Mathies, R. A. *J. Phys. Chem.* 1992, 90, 6147.

(38) Ghosh, S. N. *J. Inorg. Nucl. Chem.* 1974, 36, 2465-2466.

(39) Yang, T. S.; Westervelt, R. W.; Arnett, D. C.; Scherer, N. F. Manuscript in preparation.

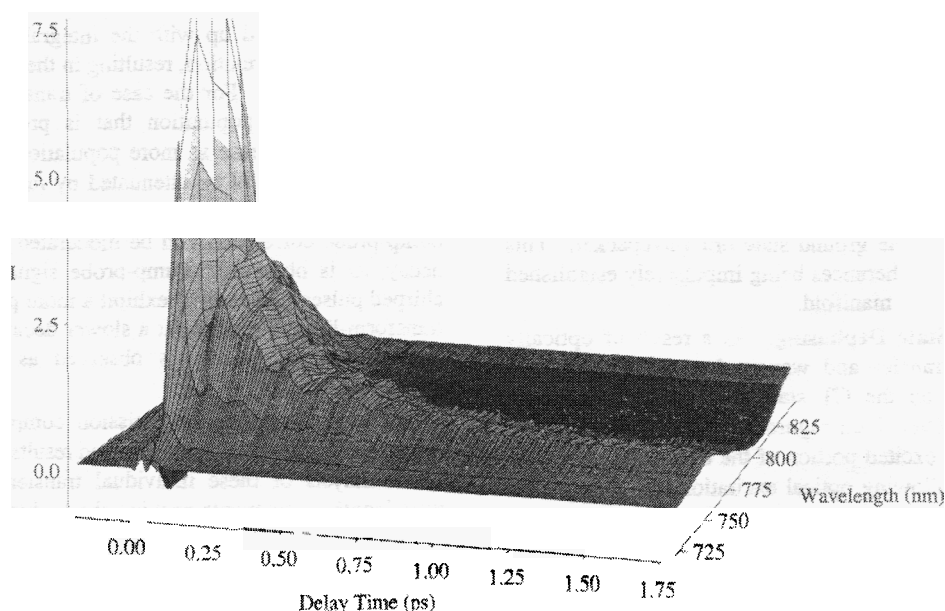


**Figure 10.** Wavelength-resolved pump-probe signal obtained with parallel polarizations. The experimental data plotted on a 3-dimensional grid give the signal intensity as a function of pump-probe delay time and 2 nm spectral bandpass every 10 nm over a spectral range of 110 nm. The grayscale is adjusted so that the ultrafast response is shown in light gray/white while the ground state bleach (pos. signal) and the oscillatory components are darker gray and the transient absorption (neg. signal) is very dark gray/black.

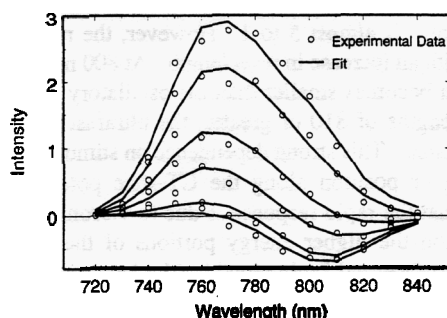


**Figure 11.** Transient differential absorption spectra at various pump-probe time delays showing the overall spectral development of the transient absorption over a 2 ps time range. The wavelength-resolved data are shown as open circles. The lines represent the fits to the individual spectra based on the kinetic model discussed in section V.C and ref no. 45.

expected to begin at shorter times for even longer wavelengths; white light probe studies to capture these dynamics are in progress.<sup>40</sup>

## V. Discussion

These experimental results may be interpreted qualitatively by considering the excitation and relaxation processes expected in optically initiated electron transfer in terms of wavepacket motion on the ground and excited CT-state potential energy surfaces. This description of four-wave mixing spectroscopies<sup>37</sup> provides a physically meaningful interpretation of the observed signals. Figure 12 shows a one-dimensional representation of the free energy surfaces for  $\text{Fe}^{\text{III}}\text{NCFe}^{\text{II}}$  (ground state) and  $\text{Fe}^{\text{II}}\text{NCFe}^{\text{III}}$  (excited state) as a function of the reaction coordinate. This figure schematically illustrates four processes contributing to the formation of the observed signals: (1) optical excitation creating a nonstationary vibronic wavepacket on the excited state, the corresponding ground state vibrational hole, and ground state vibrational coherences prepared via Raman-like processes, (2) rapid excited state (electronic) dephasing and further relaxation of the CT state, (3) transient absorption

resulting from the formation of the relaxed CT-species  $\text{Fe}^{\text{II}}\text{NCFe}^{\text{III}}$ , and (4) back electron transfer resulting in ground state bleach recovery. The following discussion is centered on how each of these processes are exhibited in the temporal and spectral characteristics of the observed signals and the molecular dynamics involved.

**A. Optical Excitation.** Upon optical excitation with vibrationally impulsive pulses (process 1 in Figure 12), a portion of the ground state population is promoted to the excited state resulting in optical charge-transfer from  $\text{Fe}^{\text{II}}$  to  $\text{Fe}^{\text{III}}$ . Two matter-radiation interactions are involved in this optically induced electron transfer. First, the pump pulse interacts with the ground state ket wavepacket promoting it to the excited state and creating an electronic coherence between the ground and excited state. Second, the pump pulse interacts with the ground state bra wavepacket promoting it to the excited state as well, creating populations and coherences in the CT excited state. In the absence of other interactions, the excited state vibronic wavepacket then evolves according to the excited state Hamiltonian.

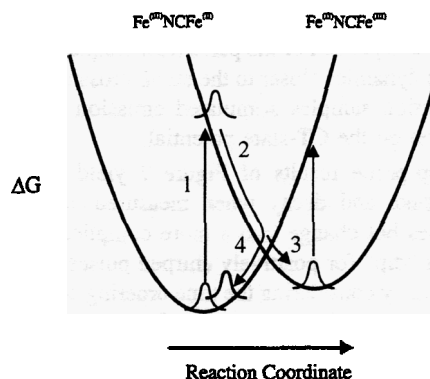


**Figure 12.** Potential energy diagram showing the excitation and relaxation processes in Prussian blue. The highlighted processes are as follows: (1) optical excitation creating an excited state wavepacket and a ground state hole, (2) rapid dephasing and relaxation of the excited state wavepacket, (3) formation of relaxed excited state species  $\text{Fe}^{\text{II}}\text{NCFe}^{\text{III}}$ , and (4) back electron transfer and ground state recovery.

(40) Arnett, D. C.; Yang, T. S.; Scherer, N. F. Manuscript in preparation.



The creation of an excited state wavepacket also results in depletion of the ground state population, leaving a nonstationary hole in the ground state vibrational wavepacket. This is sometimes referred to as a transient hole burning contribution to nonlinear spectroscopy. Ground state vibrational coherences can be excited if the second interaction with the pump pulse returns the (newly formed) excited state ket wavepacket back to the ground state. If the bandwidth of the laser pulse is sufficient, the ket wavepacket may be returned to a different vibrational level than the ground state bra wavepacket. This results in vibrational coherences being impulsively established within the ground state manifold.

**B. Rapid CT-State Dephasing.** As a result of optically induced electron transfer and wavepacket preparation to a displaced position on the CT state free energy curve, the excitation process (step 1 on Figure 12) yields a wavepacket on an energetically excited portion of the charge-transfer free-energy surface. Following optical excitation, the wavepacket will move rapidly down the free energy surface, evolving toward a more favorable configuration. The entire system, including the lattice and solvent bath, undergoes prompt relaxation in response to the new charge distribution or vibrational excitation in the "chromophore". This evolution corresponds to three physical processes: (1) electronic dephasing or spreading of the vibronic wavepacket, (2) dissipation of the vibrational multimode coherent superposition of states, and (3) relaxation due to the reorganization of the lattice, solvent, and coordinated waters. The first two processes can be understood to reduce the free energy by increasing entropy, while the third does so by decreasing the enthalpy of the system through bath friction. Both the dephasing of the initially coherent superposition of "degenerate" electronic transitions and the relaxation of the wavepacket due to solvent motions occur on rather fast time scales and give rise to the ultrafast component observed in both the  $S_{ij}(t)$  and  $r(t)$  measurements.

The assignment of the ultrafast component to excited state vibronic wavepacket motion and dephasing can be made on the basis of the chirped pulse, frequency resolved, and anisotropy measurements. Excited state wavepacket evolution may be detected through stimulated emission, which results from the probe pulse interacting with the excited state population. The stimulated emission frequency, determined by the energy difference between the ground and excited state energy surfaces, depends on the location of the excited state wavepacket on the CT-state potential surface. It then follows that the individual frequency components of the probe pulse are sensitive to dynamics on different regions of the excited state potential. For instance, the red portion of the pulse (low frequency) will probe excited state dynamics closer to the curve-crossing region while the blue portion samples stimulated emission from a higher energy region on the CT-state potential.

The pump-probe results of Figure 7 yield the prominent ultrashort spike and decay when measured with transform-limited pulses but change into a more complicated waveform containing a "dip" for positively chirped pulses. This dip can be understood by considering the time ordering of the frequency components in the chirped pulse; low frequency precedes high. If the excited state wavepacket is initially prepared with the red portion of the pulse and rapidly dephases (i.e. moves out of the probe pulse spectral range), the trailing blue edge of the probe pulse is not able to stimulate emission. Therefore, the expected waveform for degenerate frequency positively chirped pulses would exhibit enhanced stimulated emission at the time of pump-probe overlap that would rapidly diminish through

reduction of the temporal overlap, which is dictated by the coherence time of the pulses. The ground state bleach will, however, still build up with the integral of the pump-probe intensity cross-correlation, resulting in the formation of a "dip" in the total signal. For the case of transform limited pulses, the excited state population that is probed via stimulated emission will increase as more population is promoted to the excited state but will be attenuated by rapid decay processes. Hence, this signal is expected to rise with the integral of the pump-probe correlation and be moderated by the exponential decay, as is observed. Pump-probe signals with negatively chirped pulses (not shown) exhibit a more prompt rise than the transform-limited results but a slower decay due to the poorer time resolution; no dip is observed as expected for this interpretation.

The ultrafast-stimulated emission component is also very prominent in the wavelength-resolved results presented in Figure 10. Analysis of these individual transients shows that the wavelength components probing the higher energy regions of the CT-state potential are sensitive to the ultrafast component whereas those transients detected with lower energy portions of the probe pulse do not exhibit any rapid decay. The sensitivity of the individual wavelength-resolved transients to the ultrafast response can be evaluated by comparing the magnitude of the initial peak containing the rapid decay to the magnitude of the slower oscillatory responses. For detection wavelengths close to the blue edge of the pulse (730 and 740 nm) this ratio is almost 5 to 1. However, the ratio decreases steadily with an increase in wavelength. At 800 nm the ultrafast component becomes smaller than the oscillatory response, and for wavelengths of 810 or greater, the ultrafast component is not observable. This strong dependence on stimulated emission frequency, or position along the CT-state potential surface, suggests that the rapid response is due to vibronic wavepacket evolution on the higher energy portions of the excited state potential surface and "solvation" by the bath.

More information about the excited state wavepacket motion can be obtained from the anisotropy measurements. The wavelength integrated anisotropy, calculated from the deconvoluted responses and shown in Figure 8, shows a rapid decay ( $\tau = 15$  fs) to a constant level after reaching an initial peak of 0.4.<sup>41</sup> This rapid anisotropy decay occurs on the same time scale as the fast decay seen in  $S_{ij}(t)$  and the rapid rise in  $S_{\perp}(t)$  that have been attributed to excited state vibronic wavepacket evolution. Furthermore, the rapid loss of anisotropy indicates that this wavepacket motion corresponds to dephasing and orientational (spatial) delocalization of the wavepacket. In this interpretation, the initially prepared excited state wavepacket corresponds to a well oriented (localized) wavepacket formed by a coherent superposition of the electronically degenerate excited states. Rapid CT-state dephasing then corresponds to the loss of this initial electronic state coherence or wavepacket orientational delocalization. During electronic dephasing the superposition state is reduced to the incoherent sum of CT-probabilities along the three mutually orthogonal  $\text{Fe}^{\text{II}}-\text{Fe}^{\text{III}}$  directions, eventually resulting in a net isotropic excitation reflecting the octahedral symmetry of the individual wavefunctions. Following electronic dephasing, the electron is equally

(41) The decay in the rise of the deconvoluted anisotropy is also reflected in a time shift of 2–3 fs in simulations of the undeconvoluted anisotropy. We believe that this shift results from the altered distance that the pump travels following rotation of the half-waveplate due to changes in index of refraction causing "retardation". We estimate that the time shift could be as large as 2 fs for a zero-order mica waveplate. The rise of the deconvoluted data disappears if the parallel data is shifted by 2 fs earlier in time—this is the direction of the shift for our experimental geometry and polarizations.



likely to have transferred to any of the six  $\text{Fe}^{\text{III}}$  sites about each  $\text{Fe}^{\text{II}}$ . It should be noted that the remaining excited state wavepacket may still be vibrationally coherent after electronic excitation but we assume that these vibrational motions are not directly observed in the present experiments. Also, relaxation due to solvent and lattice reorganization continues to occur as the wavepacket relaxes down the CT-state potential surface, but as stated before, this bath dissipation, termed solvation, will not cause a reduction in anisotropy.

Wynne and Hochstrasser<sup>42</sup> have developed a description of anisotropy measurements for systems with energetically degenerate states with different transition moments and have applied these techniques to study the dephasing of electronic coherences. This treatment predicts that the initially prepared coherent superposition of states gives rise to anisotropies greater than the classical limit of 0.4. For a triply degenerate system, an initial anisotropy of 1 is expected, which dephases to the classical limit of 0.4. This trend has apparently been observed by Barbara and co-workers for the metal to metal charge-transfer in a  $\text{Ru}^{\text{II}}\text{--Ru}^{\text{III}}$  mixed valence dimer<sup>19</sup> where the coherent superposition of states arises from the triple degeneracy of the  $t_{2g}$ -donating and -accepting orbitals along the single bridging ligand. The diatom-like Ru case differs from Prussian blue which exhibits triply degenerate transitions between the donating  $\text{Fe}^{\text{II}}$  ion and each of the possible (equivalent) accepting  $\text{Fe}^{\text{III}}$  ions located in octahedral sites about the  $\text{Fe}^{\text{II}}$ . Anisotropies greater than 0.4 should also be observed for Prussian blue. Although larger anisotropies have not been observed via the wavelength-integrated detection scheme used to obtain Figure 8, values greater than 0.4 are expected for detection near the short wavelength edge of the pulse where the probe is most sensitive to the initially prepared coherence as discussed in the previous paragraph. Wavelength-resolved anisotropy measurements are in progress to further substantiate this interpretation of rapid delocalization.<sup>40</sup>

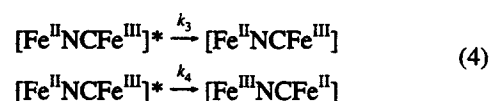
The smaller than expected initial anisotropy observed here may also result from excitation with a pulse that is detuned by 80 nm from the absorption maximum. The three  $t_{2g}$  orbitals that contribute to each CT pair ( $\text{Fe}^{\text{II}}\text{--Fe}^{\text{III}}$ ) may not be perfectly degenerate but could be split in energy. As in the case of the solvated electron,<sup>43</sup> a splitting of the transition energies could reasonably occur since each of the three orbitals has a different projection into portions of the lattice that contains water or potassium counterions at interstitial sites. This could lead to a splitting of electronic transition energies such that excitation to the red of the absorption maximum would result in a lower initial anisotropy than excitation at the absorption maximum where all three transitions are energetically possible. This explanation is consistent with the wavelength-resolved data mentioned above, where the shorter wavelength portion of the pulse is more on resonance with the transition and more sensitive to the electronic coherence. Tunable pump experiments would help to resolve this issue.

**C. Curve Crossing, Back Electron Transfer, and Transient Absorption.** Following the initial relaxation of the CT-state through electronic dephasing and orientational delocalization, the excited state wavepacket may relax further through two possible pathways: (1) back electron transfer, and (2) formation of the relaxed excited state species  $\text{Fe}^{\text{II}}\text{NCFe}^{\text{III}}$ . The wavelength of the transient absorption in Figure 11 corresponds quite well with the expected transition energy of an excited state

absorption from the charge-transfer species. These relaxation processes are labeled as processes 4 and 3, respectively, in Figure 12.

As seen in Figure 12, back electron transfer would occur by way of a crossing of the two free energy curves and would be detected through the decay of the ground state bleach signal. The bleach, which results from the depletion of the ground state population by optical excitation, is evident as the intermediate time scale response in both  $S_{\parallel}(t)$  and  $S_{\perp}(t)$  wavelength integrated transients shown in Figures 5, 7, and 10. The decay of this bleach would track the repopulation of the initial ground state distribution.

While the decay of the ground state bleach reflects the recovery of the equilibrated ground state Prussian blue population, the appearance of a persistent transient absorption can only result from the formation of a new species. The energy of the transient absorption, observed as a negative signal on the low wavelength portion of the wavelength-resolved response, corresponds very well with an optical excitation from a relaxed and persistent excited state population of  $\text{Fe}^{\text{II}}\text{NCFe}^{\text{III}}$  to the Prussian blue  $\text{Fe}^{\text{III}}\text{NCFe}^{\text{II}}$  ground state. This transition is about  $2000\text{ cm}^{-1}$  lower in energy than the absorption max associated with the MMCT from the Prussian blue ground state. The growth of the transient absorption would, therefore, monitor the formation of an excited state population in the "bottom" of the CT-state free energy well (see Figures 2 and 12). Subsequent decay of this absorptive feature would yield information about reverse electron transfer over the activation barrier distinguishing the  $\text{Fe}^{\text{II}}\text{NCFe}^{\text{III}}$  and  $\text{Fe}^{\text{III}}\text{NCFe}^{\text{II}}$  Prussian blue configurations. The validity of this interpretation of the intermediate time scale dynamics observed in Figures 5, 7, 10, and 11 and schematically illustrated in Figure 12 can be shown with a simple kinetic analysis of the dynamics. The formation of an excited state species and ground state recovery can be treated in a simple kinetic sense as a parallel first-order decay of a reactant into two different products.<sup>44</sup>



Here  $[\text{Fe}^{\text{II}}\text{NCFe}^{\text{III}}]^*$  represents the nonrelaxed (but spatially delocalized) excited state population at small delay time (i.e.  $t \approx 50\text{ fs}$ ), which decays via pathways 3 and 4 as diagrammed in Figure 12 yielding transient absorption from the relaxed CT state  $\text{Fe}^{\text{II}}\text{NCFe}^{\text{III}}$  population or bleach recovery from the recovering ground state  $\text{Fe}^{\text{III}}\text{NCFe}^{\text{II}}$ , respectively. The rate constants  $k_3$  and  $k_4$  are associated with the two relaxation mechanisms. The thermally activated electron transfer from  $\text{Fe}^{\text{II}}\text{NCFe}^{\text{III}}$  to  $\text{Fe}^{\text{III}}\text{NCFe}^{\text{II}}$  occurs on a much slower time scale and will not be considered here. Assuming the transition moments are the same for both ground state and excited state absorption, the time dependent amplitudes of the populations contributing to excited state absorption  $C_3(t)$  and ground state bleach recovery  $C_4(t)$  are given by

$$\begin{aligned} C_3(t) &= \frac{k_3[A]_0}{k_3 + k_4} [1 - \exp[-(k_3 + k_4)t]] \\ C_4(t) &= \frac{k_4[A]_0}{k_3 + k_4} [1 - \exp[-(k_3 + k_4)t]] \end{aligned} \quad (5)$$

(42) Wynne, K.; Hochstrasser, R. M. *Chem. Phys.* 1993, 171, 179–188.

(43) Schwartz, B. J.; Rossky, P. J. *Phys. Rev. Lett.* 1994, 72, 3282–3285.

(44) Steinfeld, J. I.; Francisco, J. S.; Hase, W. L. *Chemical Kinetics and Dynamics*; Prentice-Hall Inc.: New Jersey, 1989.

where  $k_3$  and  $k_4$  are the rate constants for the two pathways and  $t$  represents the temporal delay between the pulses. The temporal behavior of the amplitudes of  $C_3(t)$  and  $C_4(t)$  yield the time scales for the growth of the excited state species and recovery of the ground state.

Since the repopulation of the ground state and the formation of an excited state species are detected via different portions of the probe spectrum, the time scales for these processes may be determined by analyzing the wavelength-resolved data. To establish the relative rates of the two processes, the transient spectra are modeled by two gaussians, corresponding to the excited state absorption and the ground state bleach.<sup>45</sup>

$$S(t, \lambda) = S_{\text{abs}}(t, \lambda) + S_{\text{bleach}}(t, \lambda)$$

$$S_{\text{abs}}(t, \lambda) = C_3(t) \exp \left[ - \left( \frac{\lambda - \lambda_a}{W_a} \right)^2 \right] \quad (6)$$

$$S_{\text{bleach}}(t, \lambda) =$$

$$C_4(t=0) - C_4(t) \begin{cases} \exp \left[ - \left( \frac{\lambda - \lambda_b}{w_{b1}} \right)^2 \right]; \lambda \leq 765 \text{ nm} \\ \exp \left[ - \left( \frac{\lambda - \lambda_b}{w_{b2}} \right)^2 \right]; \lambda > 765 \text{ nm} \end{cases}$$

Here,  $t$  again represents the temporal delay between pulses,  $\lambda$  denotes the detection wavelength,  $\lambda_a$  and  $\lambda_b$  represent the center wavelengths of the observed excited state absorption and ground state bleach, respectively.  $C_3(t)$  and  $C_4(t)$  are the time dependent amplitudes of the populations contributing to transient absorption and ground state bleach recovery as given by eq 5. The results of this analysis are presented as the solid lines in Figure 11. The very good agreement between experiment and simulation indicate that this simple model for the intermediate time scale transient spectra is correct. The isosbestic expected in a two-step process is not observed. Therefore, the transient features evolve by parallel channels in the two electronic states rather than a sequential process within the Prussian blue electronic ground or excited state.

The data associated with the population amplitudes for the transient absorption and bleach recovery processes are shown as the circles on Figure 13. The fitted curves to the data, represented by the solid lines, are based on the kinetic expressions given in eqs 4–6. The independently fitted total rate constants for the bleach decay and transient absorption data are  $4.4 \pm 0.9 \text{ ps}^{-1}$  and  $3.9 \pm 0.8 \text{ ps}^{-1}$ , respectively. The good agreement of the rate constants for the two data sets further validates the appropriateness of this model since the rate constants for two parallel reaction channels are given by the total rate of depletion of reactant. However, the magnitude of the population returning to the ground state is approximately 4 times that contributing to the excited state formation, giving the relation  $k_4 \approx 4k_3$ . The best fits for the curves (solid lines in Figure 13) therefore yield  $k_3 = 0.9 \pm 0.2 \text{ ps}^{-1}$  and  $k_4 = 3.5 \pm 0.8 \text{ ps}^{-1}$ , indicating that back electron transfer is the preferred relaxation mechanism.

These observables suggest that the immediate back electron transfer occurs on a few hundred fs time scale as judged by the decay of the ground state bleach. This time scale for immediate

(45) The simulated form for the bleach consists of two half gaussians that range from 720–765 nm and 765–840 nm. This was done to more accurately capture the  $t = 100 \text{ fs}$  spectral form and provides a somewhat better fit to all of the time delay spectra than a simple symmetric gaussian for the bleach contribution to the signal. The gaussian widths are  $w_a = 26 \text{ nm}$ ,  $w_{b1} = 24 \text{ nm}$ , and  $w_{b2} = 42 \text{ nm}$ .

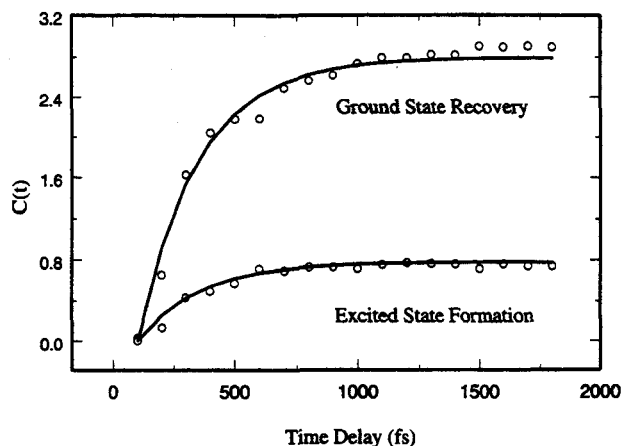


Figure 13. Time evolution of the kinetic model amplitudes corresponding to the transient excited state population and ground state recovery as a function of pulse delay time,  $C_3(t)$  and  $C_4(t)$ , respectively.

back electron transfer is on the same order of magnitude as reported for other mixed valence compounds.<sup>19</sup> Furthermore, the lack of anisotropy over these time scales suggests that the electron transfer occurs from all of the excited state  $\text{Fe}^{\text{II}}$  ions surrounding the accepting  $\text{Fe}^{\text{III}}$ .

**E. Vibrational Coherences and Dephasing.** The appearance of discrete spectral features in the Fourier transformed pump-probe signal indicate that the associated vibrational modes are coupled to the optically-initiated electron transfer process.<sup>21,22</sup> This activity results from nuclear displacements associated with the electron-transfer processes. Displacement of the vibrational modes resulting from this coupling create Franck–Condon progressions in absorption and Raman activity in the ground state.<sup>14,46</sup> Ground state vibrational coherences, established via Raman processes during the optical excitation with a femtosecond pump pulse, are observed in Figure 6 and analyzed in Figure 10. The two most prevalent coherences yield oscillations with frequencies of 70 and 270  $\text{cm}^{-1}$  as determined by Fourier transform analysis. Singular value decomposition analysis established the dephasing times for the two modes to be 60 and 600 fs, respectively. Hence, the vibrational dephasing times are similar to, but bracket, the time scale for the back electron transfer process and bleach recovery. This finding is in agreement with the work of Barbara et al. who found that vibrational coherence is maintained throughout the back electron transfer process in mixed valence dimers.<sup>19</sup> The more rapid decay of the low frequency mode agrees qualitatively with the notion that lower frequency motions are damped more quickly than high frequency modes because of greater displacements, anharmonicity in the potential, and/or larger bath density of states.<sup>34,47</sup>

Analysis of the frequency-resolved transients yields a description of the phase angle for each vibrational mode as a function of detection wavelength. This shows a monotonic increase in phase angle as the detection wavelength decreases. Further analysis of this wavelength dependent phase angle in terms of displaced harmonic oscillators and wavepacket propagation simulations is currently in progress.<sup>39</sup> These simulations will allow the determination of displacement parameters which are important input for comparison with rates expected from electron transfer theory.<sup>4–6,22</sup> The relatively few modes observed here may facilitate a direct comparison with first principles simulations of the rates for relaxation and back electron transfer that

(46) Lee, D.; Stallard, B. R.; Champion, P. M. *J. Phys. Chem.* 1984, 88, 6693.

(47) Whitnel, R.; Wilson, K.; Hynes, J. T. *J. Phys. Chem.* 1990, 94, 8625–8628.

can be determined by correlation methods.<sup>22</sup> This approach would have the advantage over other cw-Raman methods of obtaining vibrational displacements from the same measurement that directly detects the dynamics of electron transfer.

## V. Summary and Conclusions

The observations presented in this paper provide an overall description of the dynamics associated with optically induced electron transfer and relaxation in Prussian blue. Optical excitation with a femtosecond laser pulse results in (i) an electron being transferred from a  $\text{Fe}^{\text{II}}$  ion in a carbon hole to  $\text{Fe}^{\text{III}}$  ions in adjacent nitrogen holes creating a coherent excited state wavepacket, (ii) creation of a hole in the ground state population, and (iii) excitation of vibrational coherences on the ground state via Raman processes. The excited or CT-state wavepacket undergoes rapid electronic dephasing as the individual components of the excited state lose electronic coherence, and the wavepacket delocalizes through the octahedral network yielding a net isotropic excited state consisting equally of all six octahedral sites surrounding the electron-donating  $\text{Fe}^{\text{II}}$ . Population relaxation, back electron transfer, and formation of a relaxed  $\text{Fe}^{\text{II}}\text{NCFe}^{\text{III}}$  product then occur as the symmetric delocalized excited state relaxes back to the ground state or forms the excited state product. The ground electronic state contribution to the pump-probe signal exhibits vibrational coherences due to Raman excitation by the pump pulse and a decay of the optically induced bleach following back electron transfer. The measured dephasing of these coherences and a decay of the transient bleach track the recovery of the ground state population distribution. The newly formed excited state species yields a transient absorption near 810 nm that builds up on a sub-picosecond time scale and remains for more than 10 ps. The observation of these dynamical processes show the ability of polarization and frequency dependent pump probe measurements to detect wavepacket motion and ultrafast relaxation mechanisms in solution. Still, the mechanisms observed in this study warrant further investigation.

The role of delocalization in the rapid dephasing of the initially prepared wavepacket can be elucidated by looking at the wavelength-resolved anisotropy. Within the interpretation presented here, the localization of the wavepacket decreases as the initially prepared wavepacket evolves toward a more energetically favorable region of the excited state potential, i.e. orientational dephasing and relaxation occur simultaneously. The frequency-resolved anisotropy measurement would probe the localized nature and delocalization dynamics of the CT-state wavepacket as a function of position on the excited state potential. It is expected that the shorter wavelength components of the probe pulse should be sensitive to the wavepacket

dynamics prior to electronic dephasing, while the longer wavelength portions of the probe can detect the wavepacket only after dephasing has occurred. It follows then that the red portion of the probe pulse should exhibit less anisotropy than the blue portion. The frequency-resolved results and the chirped pulse anisotropies presented in this paper are consistent with this prediction. In addition, the measurement of the wavelength-resolved anisotropy is expected to produce anisotropies greater than 0.4 when probed with the shorter wavelength portion of the pulse.

A more complete dynamical description of the transient absorption feature will be studied via longer time experiments with probe pulses constructed from portions of a white light continuum. These studies will better establish the spectral character and time evolution of the transient  $\text{Fe}^{\text{II}}\text{NCFe}^{\text{III}}$  state that is being formed. This will track the evolution of the transient absorption feature over a wider spectral and temporal range. These continuum studies will also yield a more accurate description of the ground state coherences and dephasing in terms of displaced harmonic oscillators.<sup>39</sup>

The sensitivity of reaction dynamics to the solvent environment can be investigated by comparing the ultrafast dynamics of Prussian blue in both  $\text{H}_2\text{O}$  and  $\text{D}_2\text{O}$ . Solvent molecules are readily incorporated throughout the lattice structure of the extended solid<sup>48</sup> thereby restricting the choice of solvent to water. It is expected that the kinetic isotope effect exhibited in Prussian blue will be less than that observed in aqueous  $\text{Fe}^{\text{II}}/\text{Fe}^{\text{III}}$  systems due to the presence of the extended cyanide lattice. The results of preliminary measurements indicate that this is the case. A small or negligible isotope effect would indicate that the observed dynamics are determined mainly by intramolecular or inner-sphere processes rather than solvent dynamics.

Finally, substitutions of  $\text{Fe}^{\text{III}}$  with  $\text{Cr}^{\text{III}}$ ,  $\text{Ru}^{\text{III}}$ , and  $\text{Os}^{\text{III}}$  will allow modification of the energetics and the degree of electronic coupling to further study both optical electron transfer but also the slower activated process from the possible  $\text{Fe}^{\text{III}}\text{X}^{\text{II}}$  products.

**Acknowledgment.** We thank Prof. Paul Barbara and Dr. Norman Sutin for helpful discussions. We acknowledge the National Science Foundation (NYI), the University of Pennsylvania Laboratory for Research on the Structure of Matter (DMR-91-20668), and the DFG for financial support of this work. N.F.S. is the recipient of an Arnold and Mabel Beckman Fellowship and of a David and Lucille Packard Foundation Fellowship.

JA950059J

(48) Herren, F.; Fischer, P.; Ludi, A.; Halq, W. *Inorg. Chem.* 1980, 19, 956-959.